# First-Principles Insights into Vacancy-induced Thermal Conductivity Suppression in 2D $MoS_2$ and $MoSe_2$

Nurul Ahad Akil, Ning Zhang*
Department of Mechanical Engineering, Baylor University, Waco, TX 76798-7356, USA

**Abstract**

Point defects are prevalent in transition metal dichalcogenides (TMDCs) formed during high-temperature synthesis. In this work, we quantify their impact on lattice thermal transport in monolayer $MoS_2$ and $MoSe_2$ using first-principles density functional theory (DFT) coupled with solution of the phonon Boltzmann transport equations (BTE). The defects we investigated include mono- and di-chalcogen (S/Se) vacancies and mono-Mo vacancy. It is revealed that S/Se vacancies substantially suppress thermal conductivity, by ~67% for a mono-S vacancy in $MoS_2$ and by >77% for a mono-Se vacancy in $MoSe_2$. A single Mo vacancy produces the most severe degradation, reducing thermal conductivity by ~98%, far exceeding the effect of chalcogen vacancies despite expectations based on simple mass contrast. This extreme reduction arises from the removal of the Mo bonding hub, which induces pronounced local distortion and large perturbations of force constants, thereby enhancing phonon scattering and shortening mean free paths. Mode-resolved analysis further shows that in $MoS_2$, a Mo vacancy increases the relative contribution of out-of-plane acoustic (ZA) phonons, whereas the ZA contribution in $MoSe_2$ is largely unchanged. These results elucidate vacancy-induced degradation mechanisms and establish defect engineering as an effective route to tailor thermal transport in 2D materials. Unlike other computational approaches, our method accounts for scattering from both missing mass and altered force constants, enabling more accurate predictions of phonon scattering rates and mean free paths, and achieving better agreement with experimental results.

**Keywords:** Density functional theory, Thermal conductivity, Vacancy defects, 2D $MoS_2$ and $MoSe_2$

## 1. Introduction

Transition metal dichalcogenides (TMDCs) are a class of layered materials that have attracted significant attention due to their high surface-to-volume ratio and potential for diverse applications. Among them, two-dimensional (2D) TMDC semiconductors ($MX_2$, where M represents a transition metal and X denotes a chalcogen) have emerged as highly promising candidates for next-generation technologies, including electronics [1-3], memory devices [4-6], energy storage [7, 8], neuromorphic computing [9-11], photoluminescence [12-14] and optoelectronics [15, 16]. Phonon-mediated thermal transport is highly sensitive to atomic structure and material dimensions. Structural modifications, such as strain, defects, or doping, can significantly alter phonon behavior compared to the pristine material, either enhancing or suppressing thermal conductivity. A comprehensive understanding of these phonon interactions is essential for tailoring thermal properties to meet specific application requirements. In the semiconductor industry, effective thermal management is vital for minimizing device degradation and failure by optimizing heat dissipation and controlling thermal transport pathways.

Phonon scattering by point defects arises from perturbations of the harmonicity in the lattice, which can be caused by mass differences between atoms, modifications in harmonic force constants, strain fields induced by the defect, or changes in atomic radius, all of which contribute to these small perturbations [17, 18]. A theoretical framework for phonon-point-defect scattering was developed by Klemens, who derived an analytical expression for the phonon elastic scattering cross-section using second-order

perturbation theory [19]. In their model, they have included scattering by point defects, dislocations, and grain boundaries. The primary limitation of this approach is its restriction to single-atom unit cells and its inability to handle large mass variance perturbations [20]. An alternative model addressed some of these shortcomings by incorporating the mass difference term through eigenvector components corresponding to atomic displacements in the incident and final vibrational modes [21]. For vacancies, Klemens' model suggests that distortion effects can be neglected, as the primary perturbation arises from the removal of the atomic mass. However, the missing atom also alters the local strain field, which plays a critical role in phonon scattering by modifying the vibrational frequency at a given wavevector.

Despite these advantages, the relatively low carrier mobility of TMDCs compared to silicon remains a major challenge [22]. In addition, their thermal conductivity is highly sensitive to defects and doping. Vacancy defects, which are commonly observed in experiments, have a pronounced impact on both electronic and thermal properties [23-26]. Techniques such as Molecular Beam Epitaxy (MBE) and Atomic Layer Deposition (ALD) have identified sulfur (S) and selenium (Se) vacancies as the most common defects in $MoS_2$ and $MoSe_2$, respectively [27-35]. Several studies have investigated the thermal conductivity of monolayer MoS2 using computational modeling techniques, including molecular dynamics (MD) simulations and density functional theory (DFT). However, the reported values vary widely, ranging from as low as 1.25 W/m·K to as high as 530 W/m·K [36-48], largely due to differences in computational methodologies, interatomic potentials, and simulation conditions.

Complementing MD approaches, DFT-based methods have been widely used to estimate thermal conductivity through three primary approaches: the non-equilibrium Green's function (NEGF) method, the Slack equation, and the Boltzmann transport equations (BTE). For instance, NEGF with the local density approximation (LDA) has predicted a thermal conductivity of 23.2 W/m·K for monolayer $MoS_2$ [40]. Using the Slack equation with three-phonon scattering, two studies reported room-temperature thermal conductivity values of 33.6 W/m·K [41] and 29.2 W/m·K [42]. Additionally, when applying the single-mode relaxation time approximation (SMRTA) with DFT, one study determined the thermal conductivity of bulk $MoS_2$ to be $180 \pm 10$ W/m·K [46], while another study reported $90 \pm 5$ W/m·K [47]. The latter accounted for both three-phonon and isotopic scattering in the calculation, which likely contributed to the lower value. Additionally, phonon and electron drag effects can significantly influence charge and thermal transport properties in 2D semiconductors, particularly in regimes where carrier-phonon coupling is strong [49, 50].

Thermal transport in $MoSe_2$ has also been studied using both computational and experimental approaches. Experimentally, time-domain thermoreflectance (TDTR) measurements on bulk $MoSe_2$ synthesized via low-pressure chemical vapor deposition yielded a thermal conductivity of ~ 35 W/m·K [51]. In contrast, another study employing state-resolved Raman spectroscopy (ET-Raman) on mechanically exfoliated $MoSe_2$ samples (45 nm thick) reported a much lower value of $11.1 \pm 0.4$ W/m·K [52]. This significant discrepancy may stem from differences in sample preparation techniques, material purity, and the lack of precise characterization of defect concentration. Computationally, both MD and DFT have been employed to study the thermal conductivity of monolayer $MoSe_2$. Using the SW potential within the NEMD simulation, one study reported a thermal conductivity of $43.88 \pm 1.33$ W/m·K. To validate their approach, the researchers also employed the Green-Kubo equilibrium molecular dynamics (EMD) method, obtaining results within 3% of the NEMD value [53]. These findings are consistent with a DFT-based study employing the generalized gradient approximation (GGA) functional, which estimated a thermal conductivity of $17 \pm 0.5$ W/m·K for monolayer $MoSe_2$ [41]. While these studies provide valuable insights into the intrinsic thermal transport properties of monolayer $MoSe_2$, they do not explore the influence of structural defects or the microscopic mechanisms driving the reduction in thermal conductivity.

In the present work, we address this gap by systematically investigating the fundamental mechanisms governing thermal transport in TMDCs. Focusing on monolayer $MoS_2$ and $MoSe_2$, we explore the effect of common vacancy defects on heat dissipation at the atomic scale. Our study provides a comprehensive analysis of phonon-mediated energy transport, offering deeper insights into the factors that control thermal conductivity in these 2D materials.

## 2. Methodology and Simulation Setup

All DFT calculations are performed using a plane-wave basis set and the projector augmented wave (PAW) method. The Perdew-Burke-Ernzerhof (PBE) exchange-correlation functional, as implemented in the Vienna Ab initio simulation package (VASP), was employed [54, 55]. Geometric optimization of monolayer $MoS_2$ and $MoSe_2$ (space group $P6_3/mmc$) is performed using the conjugate gradient method, allowing for the relaxation of both atomic positions and cell parameters. A vacuum space of 17 Å is introduced along the *z*-axis to eliminate interactions arising from periodic boundary conditions. For geometry optimization, a 12 × 12 × 1 *k*-point mesh for the electron wave vector grid and a plane-wave energy cutoff of 600 eV were used. The total energy convergence criteria is set to $10^{-8}$ eV. The relaxed lattice parameters obtained are 3.19 Å for $MoS_2$ and 3.33 Å for $MoSe_2$, which are consistent with previous DFT reports (3.18 ± 0.01 Å for $MoS_2$ and 3.32 Å for $MoSe_2$) and experimental values (3.19 ± 0.01 Å for $MoS_2$ and 3.30 Å for $MoSe_2$).

To calculate harmonic ($2^{nd}$-order ) force constants, a 5 × 5 × 1 supercell containing 75 atoms and a 3 × 3 × 1 *k*-point mesh is used, employing the finite displacement method as implemented in PHONOPY [56, 57]. The phonon dispersion relation is derived from these $2^{nd}$-order force constants. Anharmonic ($3^{rd}$-order) force constants are then calculated using the finite difference method in Phono3py [56, 58, 59], at the Γ-point, within the same 5 × 5 × 1 supercell. A cutoff distance extending to the fifth-nearest neighbor atoms is applied. Phonon scattering is evaluated using Fermi's golden rule based on the cubic force constants. The lattice thermal conductivity is subsequently calculated using both the relaxation time approximation (RTA) and the iterative solution of the Peierls-Boltzmann transportation equation, with a 32 × 32 × 1 *q*-point mesh applied in reciprocal space [60]. To ensure numerical reliability, convergence tests are performed on both $MoS_2$ and $MoSe_2$, revealing that the computed thermal conductivity values remain effectively invariant for meshes denser than 20 × 20 × 1, as shown in Table 1. Point defects were generated by removing the Mo, S, or Se atoms from the supercell, as shown in **Fig. 1**. Each defective configuration was structurally relaxed with fixed cell volume.

Table 1. Convergence test for thermal conductivity calculation for $MoS_2$ and $MoSe_2$ using the RTA method.

| *q*-point mesh | Thermal conductivity_$MoS_2$ ($Wm^{-1}K^{-1}$) | Thermal Conductivity_$MoSe_2$ ($Wm^{-1}K^{-1}$) |
|---|---|---|
| 11×11×1 | 40.28 | 32.23 |
| 16×16×1 | 36.60 | 29.06 |
| 20×20×1 | 37.91 | 31.07 |
| 24×24×1 | 38.73 | 31.23 |
| 32×32×1 | 38.48 | 31.04 |
| 40×40×1 | 38.63 | 31.04 |

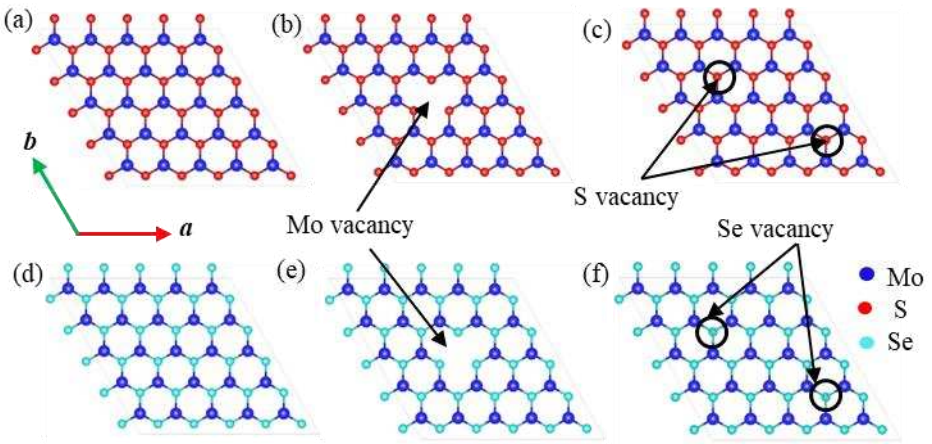


**Figure 1.** Atomic configurations of pristine and defective $MoS_2$ and $MoSe_2$ monolayers. (a) and (d) correspond to the pristine $MoS_2$ and $MoSe_2$ structures, respectively. (b) and (c) represent the $MoS_2$ and $MoSe_2$ structures with Mo vacancies, while (c) and (f) are the structures containing S and Se vacancies, respectively.

Phonon thermal conductivity ( $\kappa$ ) is calculated by [61]:

$$\kappa_{\alpha\beta} = \frac{1}{V}\sum_{\lambda} C_{\lambda}(T)\, v_{\lambda,\alpha} v_{\lambda,\beta} \tau_{\lambda} \ , \ \alpha,\beta \in \{x,y,z\} \tag{1}$$

with $\lambda \equiv (\vec{q},\vec{s})$ a phonon mode ( $\vec{q}$ : phonon wavevector and $\vec{s}$ : branch or polarization index). $C_{\lambda}(T)$ is the mode heat capacity at the temperature $T$ . $v_{\lambda,\alpha}$ and $v_{\lambda,\beta}$ represent the two group-velocity components. $\tau_{\lambda}$ is the phonon relaxation time for the mode $\lambda$ .

Electron thermal conductivity ( $\kappa_e$ ) is estimated from the Wiedemann-Franz Law,

$$\kappa_e = L\sigma T = \frac{LT}{\rho} \tag{2}$$

where $\sigma$ is the electrical conductivity, and $\rho = 1/\sigma$ is the resistivity. $L$ is the Lorenz number and is obtained as,

$$L = \frac{\pi^2}{3}\left(\frac{\kappa_B}{e}\right)^2 \approx 2.44\times10^{-8} W/\Omega\cdot K \tag{3}$$

Furthermore, the total phonon scattering rate with a vacancy defect is calculated by Matthiessen's rule:

$$\frac{1}{\tau} = \frac{1}{\tau_{anh}} + \frac{1}{\tau_b} + \frac{1}{\tau_{vac}} + \frac{1}{\tau_F} \tag{4}$$

Here $1/\tau_{anh}$ and $1/\tau_b$ are anharmonic (three-phonon) scattering and boundary scattering rates, respectively. $1/\tau_{vac}$ represents the vacancy/point-defect scattering rate, while $1/\tau_F$ denotes the force constant (bond strength) disorder with $\tau_F$ defines the lifetime limited by local force-constant disorder. In the current study, the last two terms can be determined by [19, 62-64]:

$$\frac{1}{\tau_{vac}} = \frac{\pi}{2G}\omega^2 g(\omega) x\left[\left(\frac{\Delta M}{M}\right)^2 + \varepsilon\left(\frac{\Delta r}{r}\right)^2\right] \tag{5}$$

$$\frac{1}{\tau_F} = \frac{\pi}{2G}\omega^2 g(\omega) x \left(\frac{\delta C}{C}\right)^2 \quad (6)$$

where $x$ denotes the vacancy concentration, $M$ is the host-atom mass, $\varepsilon$ is a dimensionless weight, and $\Delta M/M$ and $\Delta r/r$ represent the relative mass change and relative size/strain mismatch parameters, respectively. $g(\omega)$ denotes the phonon density of states per unit volume at $\omega$ (phonon angular frequency). $\delta C/C$ represents the relative change in local stiffness/force constants caused by the defect.

## 3. Results and Discussion

### 3.1 Phonon dispersion

Phonon dispersion relations for $MoS_2$ and $MoSe_2$ are analyzed in both pristine and defective structures, as illustrated in **Fig. 2**. A key observation is that a larger mass difference between constituent atoms leads to a broader phonon frequency range. As the mass difference between Mo and S is greater than that between Mo and Se, $MoS_2$ exhibits a higher phonon frequency range: 0 ~ 13.7 THz ($MoS_2$) vs. 0 ~ 10.4 THz ($MoSe_2$), as illustrated in **Fig. 2a, d**. In the $MoS_2$ monolayer, acoustic branches, corresponding to in-phase atomic motions, are confined below 4.7 THz. A pronounced phononic band gap is observed between 6.8 and 8.2 THz, where no vibrational states are permitted. The optical branches, associated with out-of-plane atomic motions, begin at approximately 8.2 THz. Similar to $MoS_2$, the phonon dispersion of pristine $MoSe_2$ exhibits a characteristic band gap of 0.8 THz (**Fig. 2d**). The introduction of vacancies reduces the energy separation between the phonon bands, a consequence of phonon mode softening and band broadening induced by structural disorder [65]. This effect is most pronounced in $MoSe_2$, where the vibrational spectra of structures with di-Se vacancies exhibit a complete closure of the photonic band gap in **Fig. 2f**.

Further insights from the PDOS reveal strong mixing of Mo and Se atom vibrations at low frequencies in $MoSe_2$ (**Fig. 2d**), resulting in a higher phonon scattering rate compared to MoS2 and contributing to its lower thermal conductivity. Vacancies also introduce quasi-localized phonon modes [66], appearing as additional peaks in the low-frequency region of the DOS. These modes exhibit near-zero group velocities, which diminishes phonon transport efficiency. The flattening of the phonon dispersion curves and narrowing of the frequency range upon introducing S and Se vacancies (**Fig. 2b, c, e, f**) signify phonon localization. This directly creates more available three-phonon scattering channels, leading to a further suppression of thermal conductivity. In pristine $MoS_2$, the phonon DOS is dominated by Mo atoms at low frequencies (**Fig. 2a**), whereas in $MoSe_2$, the DOS contributions from Mo and Se largely overlap due to their smaller mass difference (**Fig. 2d**). This overlap enhances phonon-phonon scattering in $MoSe_2$, providing an additional explanation for its lower thermal conductivity compared to $MoS_2$.

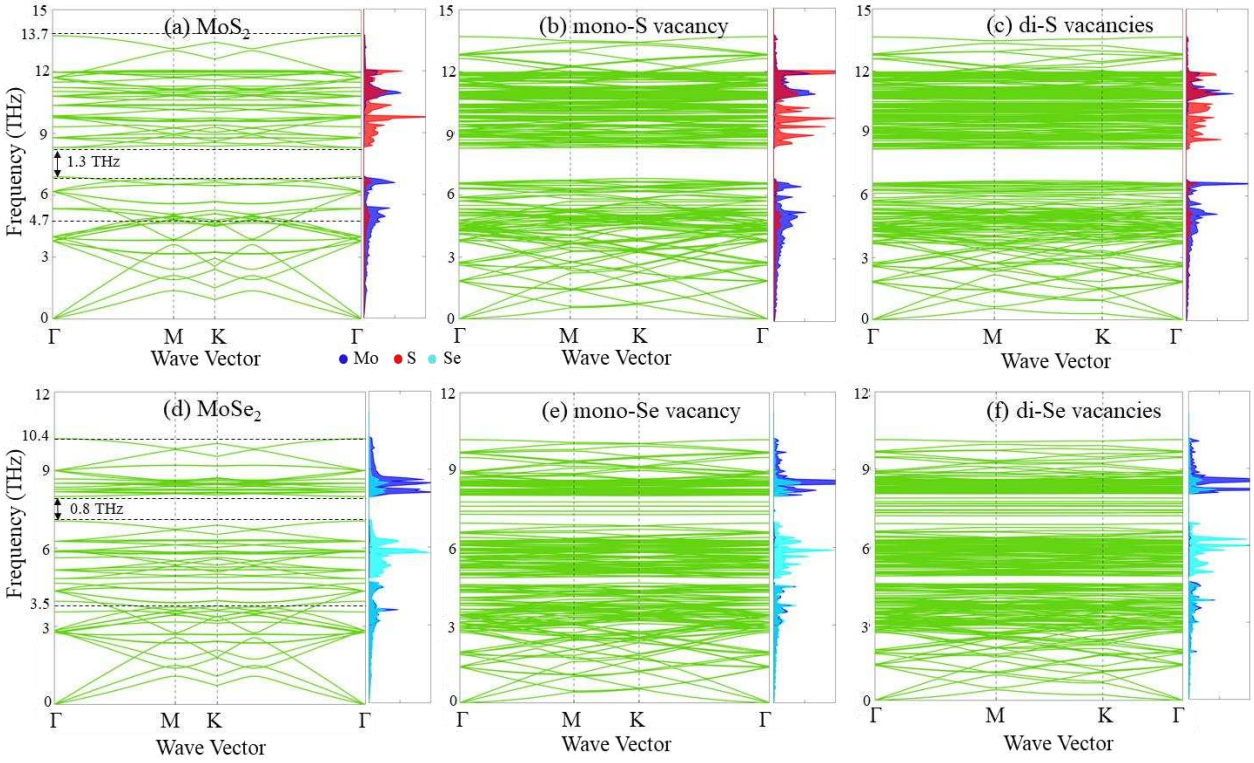


**Figure 2.** Phonon dispersion curves and phonon density of states (PDOS) for monolayers: (a) pristine $MoS_2$, (b) $MoS_2$ with mono-S vacancy, (c) $MoS_2$ with di-S vacancies, (d) pristine $MoSe_2$, (e) $MoSe_2$ with mono-Se vacancy, and (f) $MoSe_2$ with di-Se vacancies. The phonon dispersion relations are plotted along the high-symmetry directions of the Brillouin zone (Γ–M–K–Γ).

### 3.2 Electronic dispersion

The electronic band structures of monolayer $MoS_2$ and $MoSe_2$ with three different types of vacancy defects, namely, one Mo vacancy, one S vacancy, and two S vacancies, are shown in **Fig. 3a, e, c,** and **g**, and **Fig. 4a, e, c,** and **g**, respectively. Both materials exhibit direct bandgaps at the *K*-point in the Brillouin zone. For pristine $MoS_2$, the bandgap is 1.63 eV, while $MoSe_2$ displays a slightly smaller bandgap of 1.42 eV. Vacancy defects often generate localized electronic states within the bandgap, which can shift the Fermi level and reduce the effective bandgap. For instance, introducing a single S vacancy in $MoS_2$ leads to the emergence of in-gap states, reducing the bandgap from 1.63 eV (**Fig. 3a**) to approximately 0.8 eV at the Γ-point (**Fig. 3e**) and altering the Fermi level position. The introduction of the second S vacancy generates additional states, further narrowing the value to 0.38 eV, as well as a transfer to an indirect bandgap, as illustrated in **Fig. 3g**. This progressive bandgap reduction suggests that the material could eventually transition to a metallic state with more vacancies introduced, compromising its semiconducting behavior.

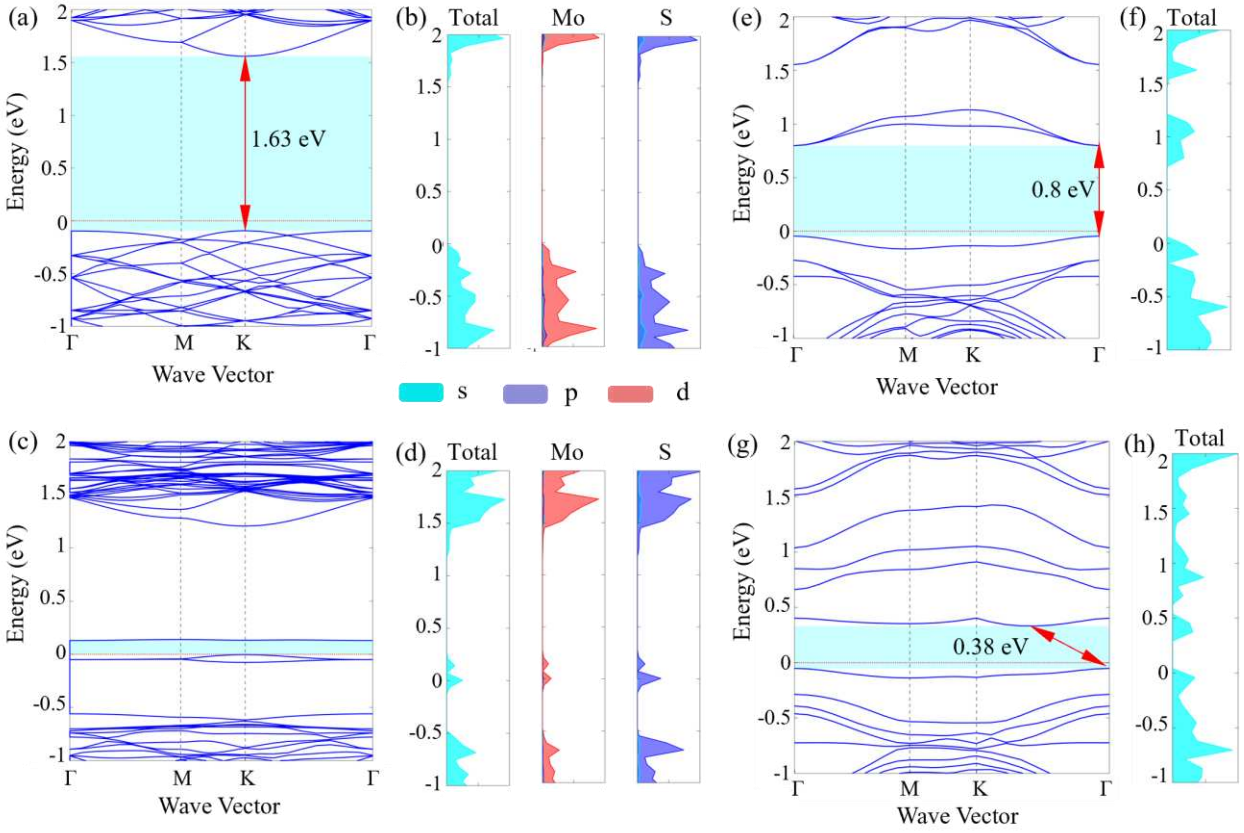


**Figure 3.** Electronic band structures and density of states (DOS) of $MoS_2$: (a, b) pristine; (c, d) with mono-Mo vacancy; (e, f) with mono-S vacancy; and (g, h) with di-S vacancies. The band gap regions are denoted by light blue shades in (a), (e), (c), and (g).

These defect-induced states typically appear as flat bands near the Fermi level due to their spatial localization. In $MoS_2$, S vacancies leave behind unpaired Mo *d*-orbitals, while Mo vacancies result in unsaturated *p*-orbitals on neighboring S atoms. The additional defect bands near the conduction band in S-defective $MoS_2$ highlight its intrinsic *n*-type characteristics. A similar trend is observed in $MoSe_2$. While the pristine monolayer exhibits a direct bandgap of 1.42 eV (**Fig. 4a**), the introduction of a single Se vacancy reduces the bandgap to 0.77 eV (**Fig. 4e**). Adding a second Se vacancy further narrows it to approximately 0.46 eV by introducing more in-gap states near the Fermi level (**Fig. 4g**). In contrast, the electronic structure exhibits a distinct response to a molybdenum vacancy (**Fig. 3c & Fig. 4c**), characterized by the emergence of new states within the band gap near the Fermi level. While the Fermi level resides within a clean band gap for pristine monolayers, the removal of a Mo atom creates unsaturated dangling bonds on the surrounding chalcogen atoms. These bonds generate localized defect states within the gap. This introduction of gap states is a clear indicator of degraded semiconductor quality, as it compromises the pristine electronic band structure.

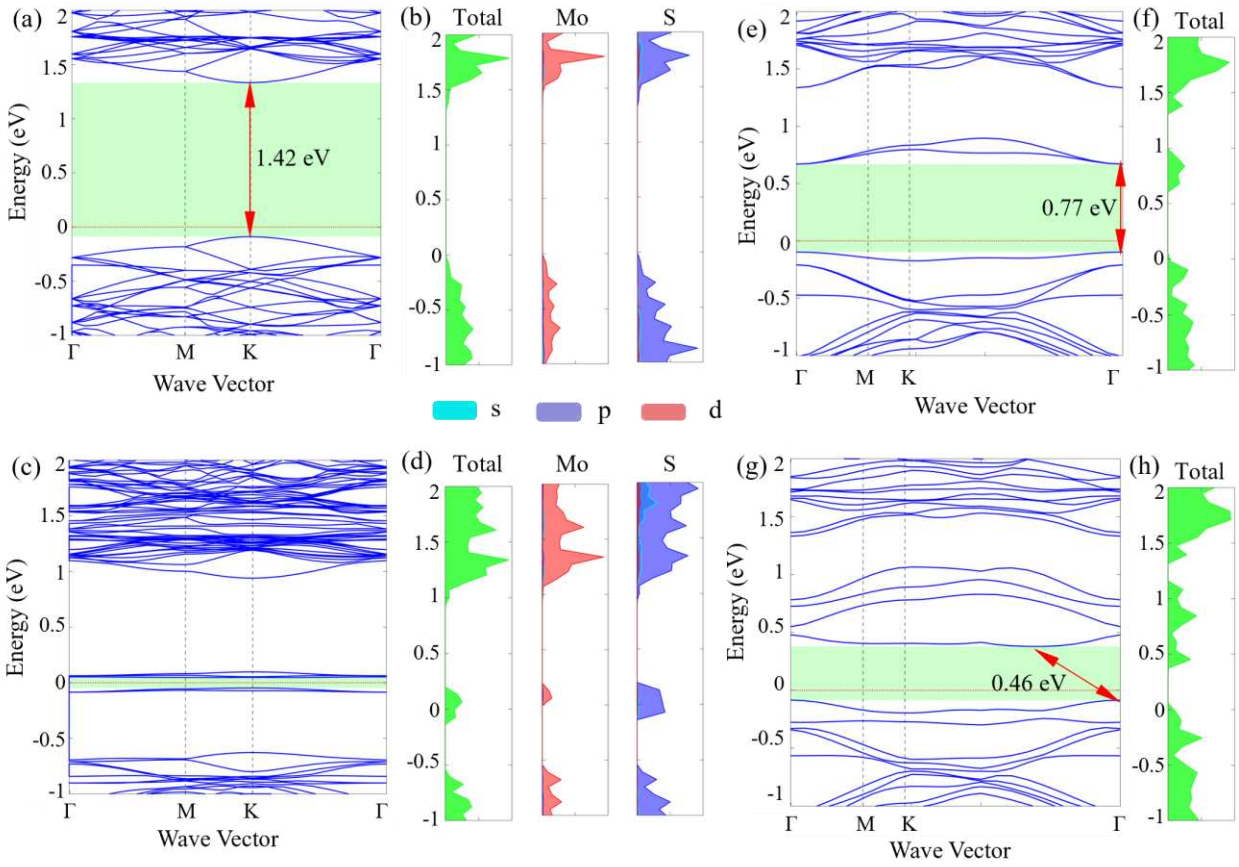


**Figure 4.** Electronic band structures and density of states (DOS) of $MoSe_2$: (a, b) pristine; (c, d) with mono-Mo vacancy; (e, f) with mono-S vacancy; and (g, h) with di-S vacancies. The band gap regions are denoted by light green shades in (a), (e), (c), and (g).

From a materials engineering perspective, these native point defects, whether arising from thermal fluctuations or introduced intentionally, can modulate the carrier concentration and enable p-type or n-type behavior, which is desirable for electronic and optoelectronic applications. However, defect formation also raises the energy of the system and thus requires activation energy, consistent with thermodynamic principles. At finite temperatures, the competing influences of enthalpy (ordering) and entropy (disordering) make the formation of a perfect crystal impossible. Consequently, defect formation is inevitable during crystal growth, regardless of the processing conditions.

### 3.3 Thermal transport behavior in $MoS_2$

The thermal conductivity of monolayer $MoS_2$ was calculated by solving the phonon BTE using both the iterative and RTA methods, as shown in **Fig. 5a**. The electronic contribution to the total thermal conductivity in pristine structures was included via the Lorentz formula. At room temperature (300 K), the calculated thermal conductivity is 54.1 W/m·K using the iterative BTE solution and 38.5 W/m·K within the RTA. All subsequent defect calculations were performed using both methods. The introduction of defects significantly reduces the thermal conductivity: a mono-S vacancy decreases it by 67.3% to 12.58 W/m·K (RTA) and 14.36 W/m·K (iterative), while di-S vacancies further reduce it to 8.89 W/m·K (RTA) and 11.05 W/m·K (iterative). The largest reduction is observed for a mono-Mo vacancy, which

lowers the thermal conductivity by 91% to 3.4 W/m·K (RTA) and 3.12 W/m·K (iterative). All configurations exhibit a consistent decreasing trend in thermal conductivity with increasing temperature.

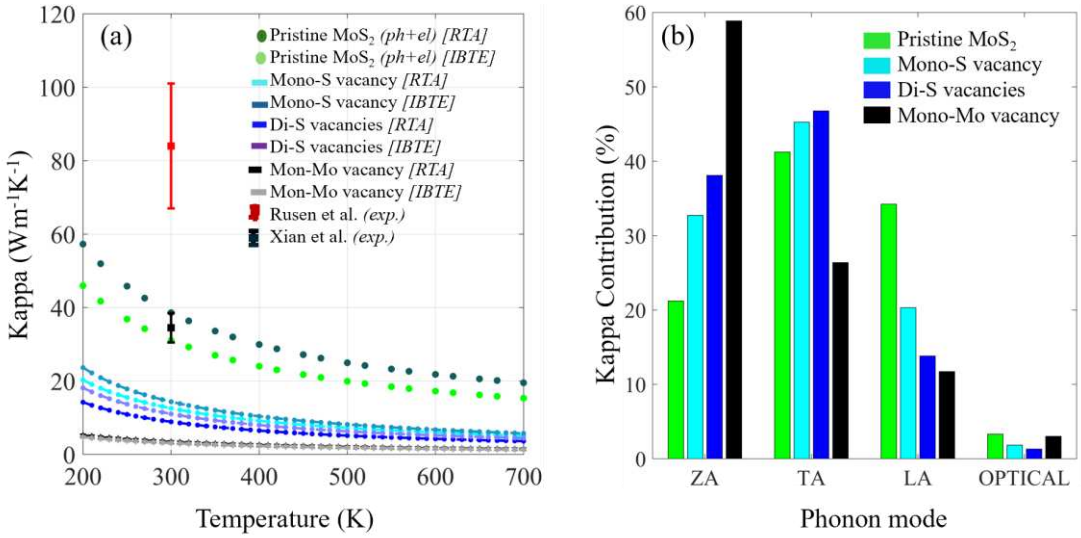


**Figure 5.** (a) Simulated thermal conductivity (lattice and electronic) of a $MoSe_2$ monolayer for pristine, mono-/di-Se vacancy, and mono-Mo vacancy configurations, compared with experimental data [67, 68]. (b) Thermal conductivity contributions resolved by individual phonon modes.

Thermal transportation in semiconductors is primarily governed by lattice vibrations, or phonons, which are quantized modes of atomic motion. Phonons are typically classified into acoustic and optical branches, with acoustic phonons, especially at low frequencies, being the primary carriers of heat. Within the acoustic phonon branch, three modes are critical: the longitudinal acoustic (LA) mode, the transverse acoustic (TA) mode, and the flexural acoustic (ZA) mode. The LA mode, or compression wave, involves atomic displacements parallel to the direction of wave propagation. The TA mode, or shear wave, involves in-plane atomic displacements perpendicular to the direction of wave travel. In contrast, the ZA mode features out-of-plane atomic displacements, causing atoms to oscillate vertically as the wave propagates.

In 2D materials, the LA and TA modes exhibit a linear dispersion relation, while the ZA mode displays a quadratic relationship near the Brillouin zone center [69]. The contribution of different phonon branches to the total thermal conductivity is detailed in **Fig. 5b**. In the pristine structure, acoustic phonons are responsible for approximately 95% of the heat transport. Among them, the transverse acoustic (TA) mode is the dominant contributor at 40%, followed by the longitudinal acoustic (LA) and the out-of-plane acoustic (ZA) modes at 33% and 21%, respectively. A notable shift in these contributions occurs with the introduction of vacancies. Specifically, the contribution from ZA phonons rises significantly, increasing from 21% in the pristine structure to 58% in the Mo-vacancy system. Given that ZA phonons are primary mediators of heat transport across 2D/3D material interfaces [69], defect engineering could be a viable strategy for manipulating thermal transport properties in van der Waals heterostructures.

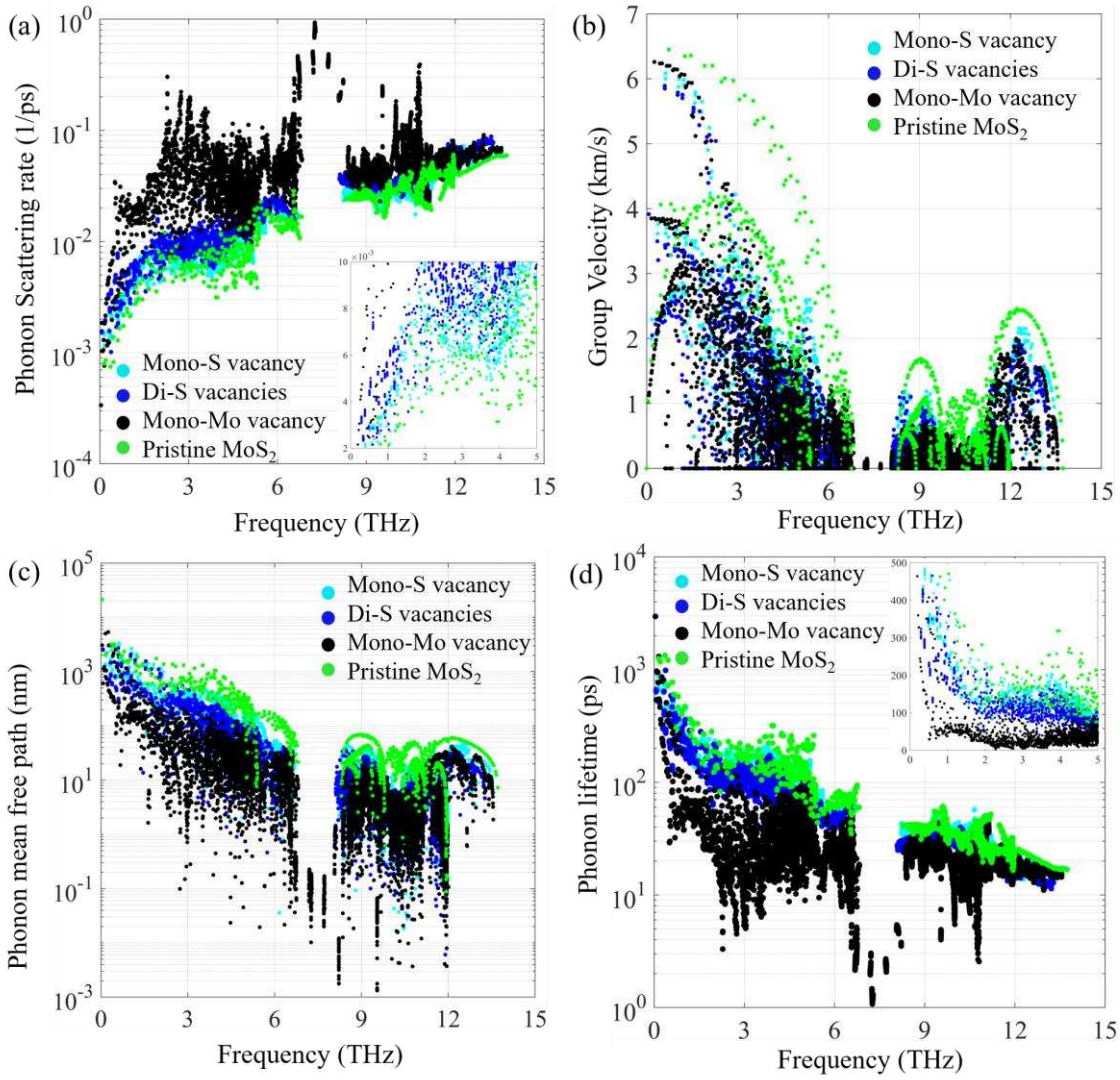


**Figure 6.** (a) Total phonon scattering rates, (b) phonon group velocity, (c) Phonon mean free path, and (d) phonon lifetime as a function of phonon frequency for the pristine structure, mono-S vacancy, di-S vacancy, and mono-Mo vacancy configurations.

Vacancy defects not only degrade thermal properties but also impact mechanical behavior by inducing local lattice strain. These defects interact most strongly with long-wavelength, low-frequency phonons, increasing scattering due to mass and elastic mismatch with the surrounding lattice. In an ideal harmonic lattice, atomic vibrations are independent, and phonon modes do not exchange energy upon interaction, making thermal conductivity theoretically temperature-independent and negating thermal expansion. However, real materials exhibit lattice anharmonicity, especially in the presence of defects, where the restoring force deviates from a linear dependence on displacement. This nonlinearity introduces energy exchange between phonons and gives rise to thermal resistance and expansion.

The phonon scattering rates for the pristine and defective structures are compared in **Fig. 6a**. Given that low-frequency acoustic phonons are the primary heat carriers (**Fig. 5b**), this region is of particular interest. At a frequency of 3 THz, the scattering rate for the pristine structure is on the order of 4 ~ 6 × $10^{-3}$/ps. The introduction of a mono-S vacancy increases this rate by approximately one order of

magnitude to the $10^{-2}$/ps region. A mono-Mo vacancy induces a more significant change, increasing the scattering rate by roughly two orders of magnitude compared to the pristine structure.

The reduction in thermal conductivity associated with S vacancies is further explained by a significant decrease in phonon group velocity within the low-frequency regime, as shown in **Fig. 6b**. This reduction signals a breakdown of harmonicity and increased phonon mode mixing [70]. While phonon branches are clearly distinguishable in the pristine structure, they become less defined in the defective systems, consistent with the observed flattening of the phonon dispersion bands. The decreased group velocity of acoustic phonons reflects lattice softening and weakened interatomic bonding, both of which contribute to reduced thermal transport efficiency. This effect is compounded by the significantly elevated phonon scattering rates in the low-frequency region for the mono-S and di-S vacancy configurations.

The observed reduction in thermal conductivity is directly governed by the fundamental scattering parameters: the phonon MFP and lifetime. The MFP defines the average distance a phonon travels before scattering, while the lifetime quantifies the time between scattering events. Our results demonstrate that these parameters are severely diminished by point defects. In pristine $MoS_2$, low-frequency phonons (0-4.5 THz), which are the primary heat carriers, exhibit a long MFP of ~1000 nm (**Fig. 6c**, green data points). The introduction of a mono-Mo vacancy induces strong structural anharmonicity, reducing the MFP by an order of magnitude to just a few hundred nanometers. This drastic reduction in travel distance directly impedes heat flow. Furthermore, a detailed comparison of phonon lifetimes (inset picture of **Fig. 6d**) reveals that defect scattering occurs much more frequently in the defective systems. This drastic reduction is exemplified at 3 THz, where the phonon lifetime decreases from 180–220 ps in the pristine structure to 80–140 ps for a di-S vacancy and further reduces to 5–40 ps for a mono-Mo vacancy. The significant shortening of both the phonon lifetime and MFP across the low-frequency spectrum is the primary mechanism behind the severe degradation of thermal conductivity in defective $MoS_2$.

### 3.4 Thermal transport behavior in $MoSe_2$

For $MoSe_2$, the lattice thermal conductivity was computed similarly, with the electronic contribution included for the pristine case (Fig. 7a). At 300 K, the RTA and iterative methods yield thermal conductivities of 31.04 W/m·K and 38.6 W/m·K, respectively. Introducing point defects leads to substantial reductions: the mono-Se vacancy decreases the conductivity by 77% to 7.09 W/m·K (RTA) and 7.63 W/m·K (iterative), while the di-Se vacancy further reduces it to 4.54 W/m·K (RTA) and 5.37 W/m·K (iterative). The most significant reduction occurs for a mono-Mo vacancy, decreasing the thermal conductivity by 98% to 0.59 W/m·K (RTA) and 0.52 W/m·K (iterative). The contribution of individual phonon modes to the total thermal conductivity is presented in **Fig. 7b**. In $MoSe_2$, low-frequency acoustic phonons are the primary heat carriers. In the pristine structure, the ZA phonon mode carries the largest share at 40%, followed by the LA mode at 38% and the TA mode at 15%. The remaining contribution is attributed to optical phonons and electrons; the electronic contribution in the defective structures was not quantified in this study. In contrast to the characteristics observed in $MoS_2$, the contribution from ZA phonons in $MoSe_2$ does not increase significantly with the introduction of vacancy defects. Furthermore, the modal contributions to thermal transport remain largely unchanged across the defective configurations studied.

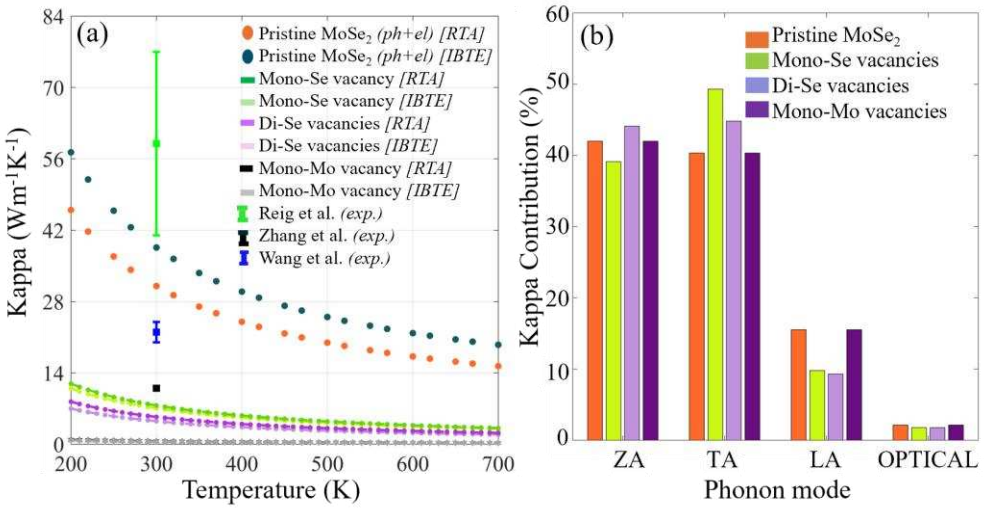


**Figure 7.** (a) Simulated thermal conductivity (lattice and electronic) of a $MoSe_2$ monolayer for pristine, mono-/di-Se vacancy, and mono-Mo vacancy configurations, compared with experimental data [52, 68, 71]. (b) Thermal conductivity contributions resolved by individual phonon modes.

To understand the mechanism behind the reduction in thermal transport due to vacancy defects, we analyzed key phonon properties: the scattering rate, group velocity, MFP, and phonon lifetime (**Fig. 8**). As shown in **Fig. 8a**, the phonon scattering rate for the pristine structure remains below 0.005 $ps^{-1}$ for frequencies up to 2.0 THz. The introduction of vacancies induces lattice distortion from the missing mass and the altered force constants between atoms surrounding the defect site. This distortion significantly increases phonon scattering. The most pronounced effect is observed in the system with a mono-Mo vacancy, which increases the scattering rate by approximately two orders of magnitude compared to the pristine structure.

A consistent trend is observed in the phonon group velocity (**Fig. 8b**). The introduction of both Se and Mo vacancies leads to a notable decline in group velocity, introducing mode mixing among low-frequency phonons, a phenomenon also observed in $MoS_2$. As these low-frequency acoustic phonons are the primary heat carriers, their reduced velocity and increased mode-mixing directly correlate with the substantial drop in thermal conductivity.

The phonon MFP results further support this conclusion (**Fig. 8c**). Low-frequency phonons in the pristine structure travel significantly longer distances before scattering than those in defective structures. For instance, at 2.2 THz, the MFP for the pristine structure ranges from 100 to 300 nm. In contrast, the introduction of a Mo vacancy drastically reduces the MFP to a range of 0.5 to 80 nm, with the majority of phonons having an MFP near 30 nm.

Finally, the phonon lifetime (or relaxation time) exhibits a pattern consistent with that observed in $MoS_2$ (**Fig. 8d**). Low-frequency phonons in the pristine structure possess lifetimes that are orders of magnitude longer than those in defective configurations. At 2 THz, the phonon lifetime for the pristine structure ranges from 140 to 320 ps, while for the structure with a Mo vacancy, it plummets to a range of 10 to 20 ps. This drastic reduction in lifetime directly demonstrates the effect of lattice distortion and the resultant changes in force constants caused by the vacancy, which enhance scattering mechanisms and degrade thermal transport.

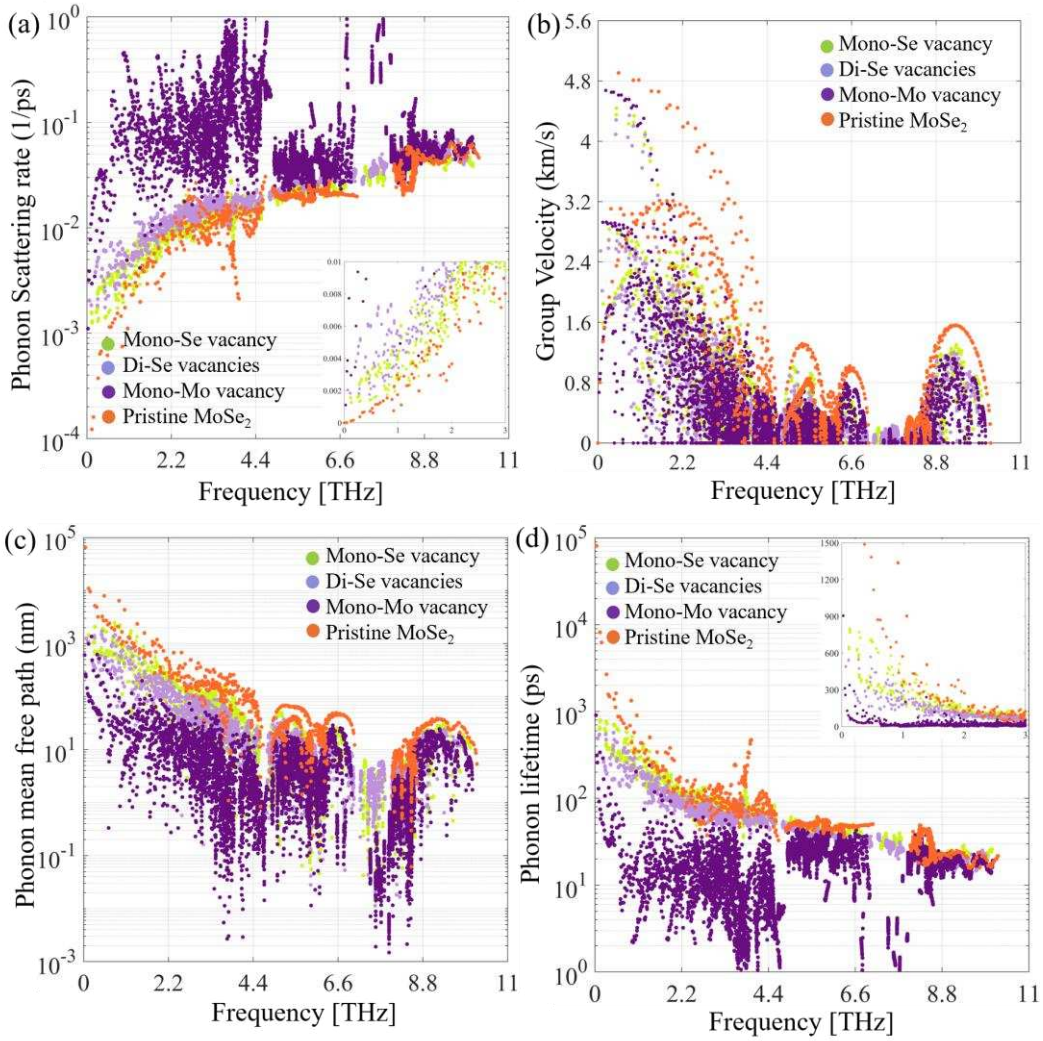


**Figure 8.** (a) Total phonon scattering rates, (b) phonon group velocity, (c) phonon mean free path, and (d) phonon lifetime of $MoSe_2$ as a function of phonon frequency for the pristine structure, mono-Se vacancy, di-Se vacancy, and mono-Mo vacancy configurations.

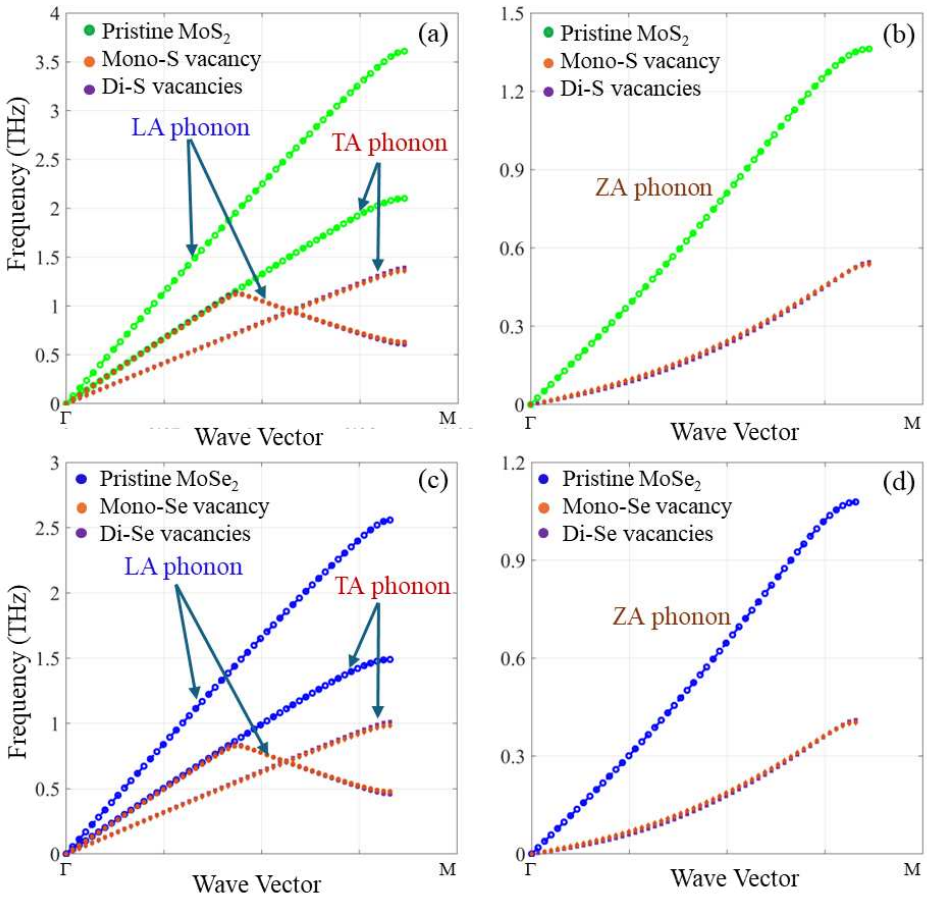


Figure 9. Phonon dispersion relations along the Γ-M direction in the Brillouin zone for pristine and defective structures. (a) and (b) show the LA, TA, and ZA phonon branches for pristine and defective $MoS_2$, respectively. (c) and (d) present the corresponding acoustic phonon branches for pristine and defective $MoSe_2$.

As acoustic phonons are the primary heat carriers in both $MoS_2$ and $MoSe_2$, we isolate the acoustic branches (LA, TA, and ZA) for detailed analysis. Fig. 9 shows that vacancy defects induce significant modifications to these branches along the Γ–M path in the Brillouin zone. Specifically, the introduction of vacancies reduces the slopes of the LA, TA, and ZA acoustic modes, indicating a decrease in phonon group velocities and elastic stiffness. This softening results from strong perturbations of phonon modes due to the removal of S/Se atoms and associated local lattice distortions. Our findings are consistent with a previous study on graphene [72], which reported similar vacancy-induced linearization of the ZA branch and a significant reduction in thermal conductivity. Therefore, our results reinforce the general understanding that point defects act as efficient phonon-scattering centers, leading to substantial reductions in lattice thermal transport across 2D materials.

## 4. Conclusion

In this work, we investigated the impact of various point defects on the thermal and electronic properties of monolayer $MoS_2$ and $MoSe_2$. Chalcogen (S/Se) vacancies preserve the semiconducting state but substantially reduce lattice thermal conductivity, whereas a Mo vacancy both disrupts semiconducting behavior and yields the largest thermal degradation (up to ~91% in $MoS_2$). The strong impact of Mo

vacancies arises from the removal of the Mo site, which induces pronounced local distortion and force-constant perturbations, thereby enhancing the phonon scattering, shortening lifetimes, and reducing mean free paths of heat-carrying acoustic modes. In contrast to other computational methods for calculating thermal conductivity, our approach includes the scattering contributions from both the missing mass and the resulting changes in force constants. This comprehensive treatment enables a more accurate capture of phonon scattering rates and mean free paths, yielding better agreement with experimental results.

Vacancies also redistribute modal contributions, with an increased relative contribution from the out-of-plane acoustic (ZA) branch in $MoS_2$. Beyond advancing the fundamental understanding of phonon-defect interactions in 2D materials, these findings have direct implications for the design of materials and devices for thermal management, thermoelectric energy conversion, and nanoelectronics, where precise control of heat flow is essential.

## Author Contributions

Methodology, software, validation, formal analysis, writing—original draft preparation, visualization: Nurul Ahad Akil; Conceptualization, methodology, writing—review and editing, supervision, project administration, funding acquisition: Ning Zhang; All authors have read and agreed to the published version of the manuscript.

## Acknowledgments

This work was supported by the National Science Foundation under Award Numbers DMR-2316676 and CMMI-2302981. Simulations were performed at the ACCESS national supercomputer center.

## Data Availability Statement

The data that support the findings of this study are available from the corresponding author upon reasonable request.

## Conflicts of interest

The authors declare that they have no known competing financial interests or personal relationships that could have appeared to influence the work reported in this paper.

## References

1. Das, S., et al., *Transistors based on two-dimensional materials for future integrated circuits.* Nature Electronics, 2021. **4**(11): p. 786-799.
2. Illarionov, Y.Y., et al., *The role of charge trapping in MoS2/SiO2 and MoS2/hBN field-effect transistors.* 2D Materials, 2016. **3**(3): p. 035004.
3. Sebastian, A., et al., *Benchmarking monolayer MoS2 and WS2 field-effect transistors.* Nature Communications, 2021. **12**(1): p. 693.
4. Zhang, F., et al., *Electric-field induced structural transition in vertical MoTe2- and Mo1–xWxTe2-based resistive memories.* Nature Materials, 2019. **18**(1): p. 55-61.

5. Bertolazzi, S., et al., *Nonvolatile Memories Based on Graphene and Related 2D Materials.* Advanced Materials, 2019. **31**(10): p. 1806663.
6. Tang, B., et al., *Wafer-scale solution-processed 2D material analog resistive memory array for memory-based computing.* Nature Communications, 2022. **13**(1): p. 3037.
7. Hu, J., S. Zhang, and B. Tang, *2D filler-reinforced polymer nanocomposite dielectrics for high-k dielectric and energy storage applications.* Energy Storage Materials, 2021. **34**: p. 260-281.
8. Nan, J., et al., *Nanoengineering of 2D MXene-Based Materials for Energy Storage Applications.* Small, 2021. **17**(9): p. 1902085.
9. Shi, Y., et al., *Electronic synapses made of layered two-dimensional materials.* Nature Electronics, 2018. **1**(8): p. 458-465.
10. Cao, G., et al., *2D Material Based Synaptic Devices for Neuromorphic Computing.* Advanced Functional Materials, 2021. **31**(4): p. 2005443.
11. Arnold, A.J., et al., *Mimicking Neurotransmitter Release in Chemical Synapses via Hysteresis Engineering in MoS2 Transistors.* ACS Nano, 2017. **11**(3): p. 3110-3118.
12. Splendiani, A., et al., *Emerging Photoluminescence in Monolayer MoS2.* Nano Letters, 2010. **10**(4): p. 1271-1275.
13. Yang, R., et al., *2D Transition Metal Dichalcogenides for Photocatalysis.* Angewandte Chemie, 2023. **135**(13): p. e202218016.
14. Yang, R., et al., *Photocatalysis with atomically thin sheets.* Chemical Society Reviews, 2023. **52**(22): p. 7687-7706.
15. Meng, Y., et al., *Photonic van der Waals integration from 2D materials to 3D nanomembranes.* Nature Reviews Materials, 2023. **8**(8): p. 498-517.
16. *Virtual Issue on Metal-Halide Perovskite Nanocrystals—A Bright Future for Optoelectronics.* Chemistry of Materials, 2017. **29**(21): p. 8915-8917.
17. Gurunathan, R., et al., *Analytical Models of Phonon--Point-Defect Scattering.* Physical Review Applied, 2020. **13**(3): p. 034011.
18. Deskins, W.R., et al., *Thermal conductivity of ThO2: Effect of point defect disorder.* Journal of Applied Physics, 2021. **129**(7): p. 075102.
19. Klemens, P.G., *The Scattering of Low-Frequency Lattice Waves by Static Imperfections.* Proceedings of the Physical Society. Section A, 1955. **68**(12): p. 1113.
20. Malekpour, H., et al., *Thermal conductivity of graphene with defects induced by electron beam irradiation.* Nanoscale, 2016. **8**(30): p. 14608-14616.
21. Tamura, S.-i., *Isotope scattering of dispersive phonons in Ge.* Physical Review B, 1983. **27**(2): p. 858-866.
22. Cheng, L., C. Zhang, and Y. Liu, *Why Two-Dimensional Semiconductors Generally Have Low Electron Mobility.* Physical Review Letters, 2020. **125**(17): p. 177701.
23. Polanco, C.A., et al., *Defect-limited thermal conductivity in ${\mathrm{MoS}}_{2}$.* Physical Review Materials, 2020. **4**(1): p. 014004.
24. Mahendran, S., et al., *Quantitative Predictions of the Thermal Conductivity in Transition Metal Dichalcogenides: Impact of Point Defects in MoS2 and WS2 Monolayers.* The Journal of Physical Chemistry C, 2024. **128**(4): p. 1709-1716.
25. Zhao, Y., et al., *Modification of thermal transport in few-layer MoS2 by atomic-level defect engineering.* Nanoscale, 2021. **13**(26): p. 11561-11567.
26. Ma, J.-J., et al., *Thermal transport properties of monolayer MoSe2 with defects.* Physical Chemistry Chemical Physics, 2020. **22**(10): p. 5832-5838.
27. Addou, R., L. Colombo, and R.M. Wallace, *Surface Defects on Natural MoS2.* ACS Applied Materials & Interfaces, 2015. **7**(22): p. 11921-11929.

28. Liu, X., et al., *Point Defects and Grain Boundaries in Rotationally Commensurate MoS2 on Epitaxial Graphene.* The Journal of Physical Chemistry C, 2016. **120**(37): p. 20798-20805.
29. Mitterreiter, E., et al., *The role of chalcogen vacancies for atomic defect emission in MoS2.* Nature Communications, 2021. **12**(1): p. 3822.
30. Vancsó, P., et al., *The intrinsic defect structure of exfoliated MoS2 single layers revealed by Scanning Tunneling Microscopy.* Scientific Reports, 2016. **6**(1): p. 29726.
31. Hus, S.M., et al., *Observation of single-defect memristor in an MoS2 atomic sheet.* Nature Nanotechnology, 2021. **16**(1): p. 58-62.
32. Zhao, Y., et al., *Electrical spectroscopy of defect states and their hybridization in monolayer MoS2.* Nature Communications, 2023. **14**(1): p. 44.
33. Liu, H., et al., *Line and Point Defects in MoSe2 Bilayer Studied by Scanning Tunneling Microscopy and Spectroscopy.* ACS Nano, 2015. **9**(6): p. 6619-6625.
34. Lehtinen, O., et al., *Atomic Scale Microstructure and Properties of Se-Deficient Two-Dimensional MoSe2.* ACS Nano, 2015. **9**(3): p. 3274-3283.
35. Chang, Y.-H., et al., *Monolayer MoSe2 Grown by Chemical Vapor Deposition for Fast Photodetection.* ACS Nano, 2014. **8**(8): p. 8582-8590.
36. Liu, X., et al., *Phonon thermal conductivity of monolayer MoS2 sheet and nanoribbons.* Applied Physics Letters, 2013. **103**(13): p. 133113.
37. Zhang, J., et al., *Phonon Thermal Properties of Transition-Metal Dichalcogenides MoS2 and MoSe2 Heterostructure.* The Journal of Physical Chemistry C, 2017. **121**(19): p. 10336-10344.
38. Xu, K., et al., *Thermal transport in ${\mathrm{MoS}}_{2}$ from molecular dynamics using different empirical potentials.* Physical Review B, 2019. **99**(5): p. 054303.
39. Wang, X. and A. Tabarraei, *Phonon thermal conductivity of monolayer MoS2.* Applied Physics Letters, 2016. **108**(19): p. 191905.
40. Cai, Y., et al., *Lattice vibrational modes and phonon thermal conductivity of monolayer MoS${}_{2}$.* Physical Review B, 2014. **89**(3): p. 035438.
41. Peng, B., et al., *Thermal conductivity of monolayer MoS2, MoSe2, and WS2: interplay of mass effect, interatomic bonding and anharmonicity.* RSC Advances, 2016. **6**(7): p. 5767-5773.
42. Su, J., et al., *Effect of temperature on thermal properties of monolayer MoS2 sheet.* Journal of Alloys and Compounds, 2015. **622**: p. 777-782.
43. Li, W., J. Carrete, and N. Mingo, *Thermal conductivity and phonon linewidths of monolayer MoS2 from first principles.* Applied Physics Letters, 2013. **103**(25): p. 253103.
44. Gu, X. and R. Yang, *Phonon transport in single-layer transition metal dichalcogenides: A first-principles study.* Applied Physics Letters, 2014. **105**(13): p. 131903.
45. Gandi, A.N. and U. Schwingenschlögl, *Thermal conductivity of bulk and monolayer MoS2.* Europhysics Letters, 2016. **113**(3): p. 36002.
46. Cepellotti, A., et al., *Phonon hydrodynamics in two-dimensional materials.* Nature Communications, 2015. **6**(1): p. 6400.
47. Lindroth, D.O. and P. Erhart, *Thermal transport in van der Waals solids from first-principles calculations.* Physical Review B, 2016. **94**(11): p. 115205.
48. Kandemir, A., et al., *Thermal transport properties of MoS2 and MoSe2 monolayers.* Nanotechnology, 2016. **27**(5): p. 055703.
49. Quan, Y. and B. Liao, *Electron Drag Effect on Thermal Conductivity in Two-Dimensional Semiconductors.* Nano Letters, 2024. **24**(26): p. 8143-8150.
50. Protik, N.H. and B. Kozinsky, *Electron-phonon drag enhancement of transport properties from a fully coupled ab initio Boltzmann formalism.* Physical Review B, 2020. **102**(24): p. 245202.

51. Jiang, P., et al., *Probing Anisotropic Thermal Conductivity of Transition Metal Dichalcogenides MX2 (M = Mo, W and X = S, Se) using Time-Domain Thermoreflectance.* Advanced Materials, 2017. **29**(36): p. 1701068.
52. Wang, R., et al., *Measurement of the thermal conductivities of suspended MoS2 and MoSe2 by nanosecond ET-Raman without temperature calibration and laser absorption evaluation.* Nanoscale, 2018. **10**(48): p. 23087-23102.
53. Hong, Y., J. Zhang, and X.C. Zeng, *Thermal Conductivity of Monolayer MoSe2 and MoS2.* The Journal of Physical Chemistry C, 2016. **120**(45): p. 26067-26075.
54. Kresse, G. and J. Furthmüller, *Efficiency of ab-initio total energy calculations for metals and semiconductors using a plane-wave basis set.* Computational Materials Science, 1996. **6**(1): p. 15-50.
55. Perdew, J.P., K. Burke, and M. Ernzerhof, *Generalized Gradient Approximation Made Simple.* Physical Review Letters, 1996. **77**(18): p. 3865-3868.
56. Togo, A., et al., *Implementation strategies in phonopy and phono3py.* Journal of Physics: Condensed Matter, 2023. **35**(35): p. 353001.
57. Togo, A., *First-principles Phonon Calculations with Phonopy and Phono3py.* Journal of the Physical Society of Japan, 2022. **92**(1): p. 012001.
58. Togo, A., L. Chaput, and I. Tanaka, *Distributions of phonon lifetimes in Brillouin zones.* Physical Review B, 2015. **91**(9): p. 094306.
59. Chaput, L., *Direct Solution to the Linearized Phonon Boltzmann Equation.* Physical Review Letters, 2013. **110**(26): p. 265506.
60. Torres, P., et al., *Thermal conductivity and phonon hydrodynamics in transition metal dichalcogenides from first-principles.* 2D Materials, 2019. **6**(3): p. 035002.
61. Chen, G., *Nanoscale energy transport and conversion: a parallel treatment of electrons, molecules, phonons, and photons*. 2005: Oxford university press.
62. Ratsifaritana, C.A. and P.G. Klemens, *Scattering of phonons by vacancies.* International Journal of Thermophysics, 1987. **8**(6): p. 737-750.
63. Klemens, P.G. and D.F. Pedraza, *Thermal conductivity of graphite in the basal plane.* Carbon, 1994. **32**(4): p. 735-741.
64. Xie, G., et al., *A Bond-order Theory on the Phonon Scattering by Vacancies in Two-dimensional Materials.* Scientific Reports, 2014. **4**(1): p. 5085.
65. Nguyen, K.T. and M. Shim, *Role of Covalent Defects on Phonon Softening in Metallic Carbon Nanotubes.* Journal of the American Chemical Society, 2009. **131**(20): p. 7103-7106.
66. Londero, E., et al., *Vibrational modes of negatively charged silicon-vacancy centers in diamond from ab initio calculations.* Physical Review B, 2018. **98**(3): p. 035306.
67. Yan, R., et al., *Thermal Conductivity of Monolayer Molybdenum Disulfide Obtained from Temperature-Dependent Raman Spectroscopy.* ACS Nano, 2014. **8**(1): p. 986-993.
68. Zhang, X., et al., *Measurement of Lateral and Interfacial Thermal Conductivity of Single- and Bilayer MoS2 and MoSe2 Using Refined Optothermal Raman Technique.* ACS Applied Materials & Interfaces, 2015. **7**(46): p. 25923-25929.
69. Foss, C.J. and Z. Aksamija, *Quantifying thermal boundary conductance of 2D–3D interfaces.* 2D Materials, 2019. **6**(2): p. 025019.
70. Shen, C.-P., et al., *Strong tunable phonon-phonon interactions induced by silicon-vacancy centers in one-dimensional chiral phononic waveguides.* Physical Review A, 2022. **106**(2): p. 023717.
71. Saleta Reig, D., et al., *Unraveling Heat Transport and Dissipation in Suspended MoSe2 from Bulk to Monolayer.* Advanced Materials, 2022. **34**(10): p. 2108352.
72. Bouzerar, G., et al., *Drastic effects of vacancies on phonon lifetime and thermal conductivity in graphene.* Journal of Physics: Condensed Matter, 2020. **32**(29): p. 295702.